Strength and deflection behaviour of cold-formed steel back-to-back channels

Jun Ye[a,c,*], Seyed Mohammad Mojtabaei[b], Iman Hajirasouliha[b], Paul Shepherd[a], Kypros Pilakoutas[b]

[a] Department of Architecture and Civil Engineering, University of Bath, Bath BA2 7AY, UK
[b] Department of Civil Engineering and Structural Engineering, The University of Sheffield, Sheffield S1 3JD, UK
[c] Faculty of Engineering & Technology, Division of Civil and Engineering, University of West of England, Bristol, BS16 1QY, UK

ABSTRACT

Cold-formed steel (CFS) construction can lead to more efficient designs compared to hot-rolled steel members as a consequence of its high strength, light weight, ease of fabrication, and flexibility in their cross-section profiles. However, CFS members are vulnerable to local, distortional and overall buckling modes. This paper develops a numerical model to investigate the flexural strength and failure modes of CFS back-to-back channel beams and verifies the efficiency of an optimisation framework previously proposed. The model incorporates non-linear stress-strain behaviour and enhanced corner properties obtained from coupon tests, as well as initial geometric imperfections measured in physical specimens. To simulate the behaviour of a bolt bearing against a steel plate in the back-to-back section, a connector model is used that takes into account both slippage and bearing deformations. The developed Finite Element (FE) models are verified against six four-point bending tests on CFS back-to-back channel beams, where excellent agreement is found between the experimental results and the FE predictions. The validated FE models are then used to assess the adequacy of the effective width method in EC3 and the Direct Strength Method (DSM) in estimating the design capacity of conventional and optimum design CFS channel beam sections. The results indicate that both EC3 and DSM provide accurate predictions for the bending capacity of lipped channel beam sections. A comparison between FE predictions and tested results show that, the geometric imperfections can change the FE predictions of ultimate capacity by 7%, while the strain-hardening of CFS material at the round corners has negligible effects. It is also shown that EC3 uses a reduced cross-sectional property to calculate deflections, which can reasonably predict deflections with a slight over-estimation (6%) at the serviceability load level.

1. Introduction

Cold-formed steel (CFS) members have traditionally been employed as load-carrying members in a wide range of applications, such as roof purlins and structural envelopes. In recent years, however, CFS members have become increasingly popular in low- to mid-rise multi-storey buildings [1] and CFS portal frames with short to intermediate spans [2,3], as shown in Fig. 1(a) and (b). CFS sections are increasingly being offered as an alternative to hot-rolled steel elements since they provide greater flexibility in terms of cross-sectional profiles and sizes, which can lead to more efficient design solutions with less redundant material. CFS sections are also light-weight, easy to handle on site, and easier to connect. However, CFS components are made of thin plates, which have inherently low buckling resistance. This results in reduced strength for CFS elements, which limits their performance in multi-storey applications. CFS components are usually susceptible to local, distortional and global buckling (and their interactions) as shown in Fig. 2.

Although the accurate prediction of the behaviour of CFS elements is difficult due to their complex failure modes, Finite Element Analysis (FEA) is widely used to predict the flexural behaviour of CFS beams [4]. Previously, a series of physical experiments on hat and back-to-back lipped beams have been conducted by Peköz et al. [5,6] to investigate the capacity of edge stiffeners in CFS sections. Compared to physical experiments, FEA is relatively inexpensive and time efficient, especially when a parametric study of cross-section geometry is involved. In addition, FEA can be efficiently used for investigations considering geometric imperfections and material nonlinearity of structural members, which could be difficult to achieve through physical tests.

---

* Corresponding author.
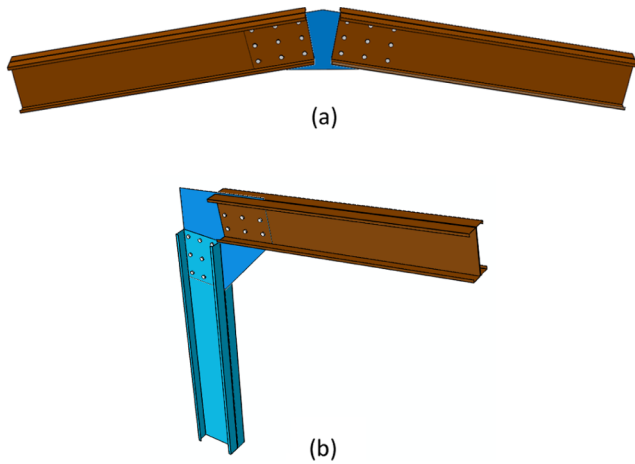*E-mail addresses:* j.ye@bath.ac.uk, zjuyejun@gmail.com (J. Ye).

Fig. 1. CFS (a) apex and (b) eaves connections with back-to-back beam sections used in typical portal frames.

Although FEA is a useful and powerful tool for the analysis of CFS structures, it is important to obtain accurate and reliable finite element models (FEM) prior to any analytical investigations. For example, Yu and Schafer [7] used nonlinear finite element models of CFS beams to develop the Direct Strength Method (DSM) design recommendations. Haidarali and Nethercot [8] then developed a simplified numerical model that could significantly increase the computational efficiency of the non-linear analyses. In their study, the geometrical imperfection of CFS profiles was determined by using the constrained finite strip software CUFSM [9], while the imperfection amplitudes were based on the statistic results presented by Schafer and Peköz [10].

In another study, Kankanamge and Mahen [11] investigated the behaviour of CFS beams subjected to lateral-torsional buckling. A detailed parametric study was conducted to simulate the lateral–torsional buckling behaviour using four-node shell elements with five degrees of freedom per node and reduced integration (S4R) in ABAQUS [12]. The results of their study were used to verify the design guidelines for the lateral-torsional buckling of CFS beams in AS/NZS 4600 [13], DSM [14] and EC3 [15]. Poologanathan and Mahen [16] developed a numerical model in ABAQUS using the S4R5 element. The numerical model was used to investigate the shear buckling and post-buckling characteristics of an innovative LiteSteel Beam. Ayhan and Schafer [17] used an experimentally verified numerical model in ABAQUS [12] to obtain a simplified method for predicting the bending stiffness of CFS members. Based on both experimental and numerical results, new local/distortional slenderness-based design equations were proposed. Similarly, Dubina et al. [18] developed an FE model to investigate the behaviour

of CFS beams with corrugated web and discrete web-to-flange fasteners. They used four-node shell elements to model the CFS components, while the connector element CONN3D2 with six degrees of freedom per node was employed in ABAQUS [12] to simulate the behaviour of self-tapping screws and bolts according to single-lap tests [19]. In a more recent study, Wang and Young [20,21] proposed a numerical model to investigate the flexural behaviour of CFS built-up sections with intermediate stiffeners subjected to bending. The S4R shell element and C3D8R solid elements in ABAQUS [12] were used to model the CFS sections and screws, respectively. The surfaces of the solid screws were tied to the drilled hole edges of the beam specimens, while surface interactions between the overlapped elements of the built-up sections were modelled using contact elements.

This paper aims to develop an advanced numerical model to predict the flexural behaviour and bending strength of CFS beam sections CFS back-to-back channel beams and to verify an optimisation framework previously proposed. An experimental investigation, including six physical tests on CFS back-to-back channel beams, which failed by local/distortional buckling about the major axis, is used to verify the FE models in ABAQUS [12]. The advantage of the developed models over the previous studies is that it incorporates non-linear stress-strain behaviour and enhanced material properties based on coupon tests, measured initial imperfections and an effective connector element to model the bolt behaviour. The models are then used to assess the adequacy of both the EC3 design guides [15,22,23] and the Direct Strength Method (DSM) to design a range of conventional and optimum designed CFS beams considering local/distortional buckling modes. The deflection of CFS beams incorporating the effects of the material non-linearity, effective cross-sections and the change of Young's modulus along the distribution of bending moment in the beams, is also investigated.

2. Eurocode 3 design formulation

Prior to the description of the numerical study, a brief introduction is presented to show how the Eurocode 3 design guidelines consider local and distortional buckling modes and their interaction on CFS beam sections.

2.1. Local buckling

In Eurocode 3, the effect of local buckling is considered through the effective width concept. It is based on the observation that local buckling causes a loss of compressive stiffness in the centre of a plate supported along two longitudinal edges ('internal' plate element), or along the free edge of a plate supported along one longitudinal edge ('outstand' plate element) as a result of non-linear effects. The corner
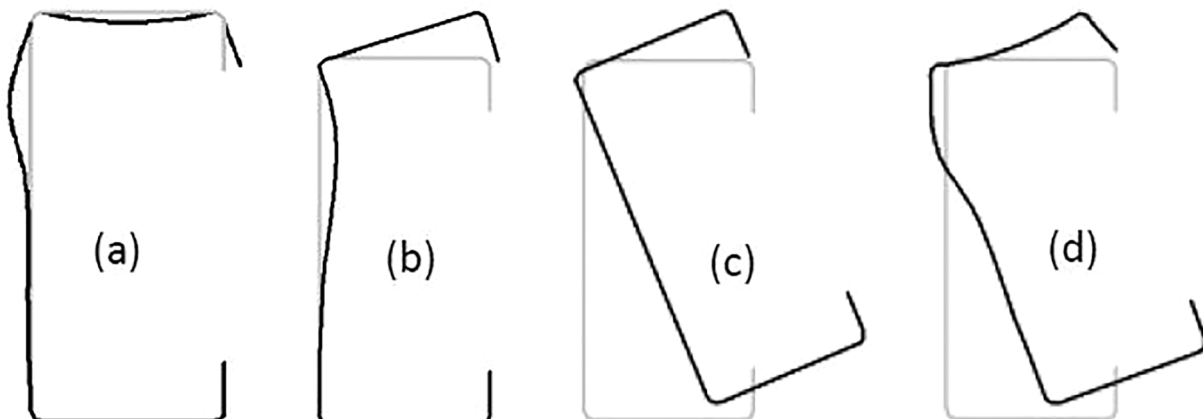

Fig. 2. Buckling of a lipped channel beam: (a) local, (b) distortional, (c) lateral-torsional and (d) local-global interactive modes.
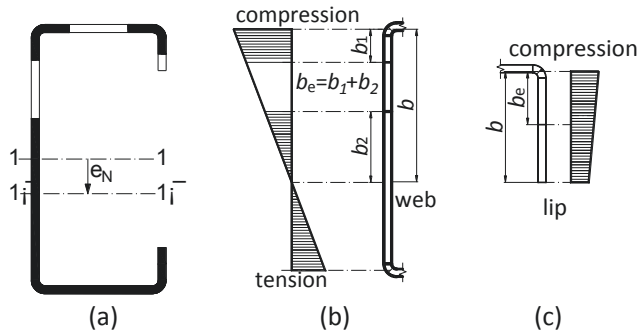
Fig. 3. Effective width of (a) lipped channel; (b) internal compression element; and (c) outstand compression element (the lip).

zones of the cross-section consequently become the main load-bearing areas and are idealized in the effective width concept to carry the total load. The effective area of a sample cross-section is indicated in solid black line in Fig. 3. It is thereby noted that local buckling causes the centroid of the effective cross-section to shift over a distance e_N relative to the original centroid of the gross cross-section. According to EC3, Part 1.5 [22], the effective widths of internal and outstand compression elements are given by (see Fig. 3):

$$\rho = \frac{b_e}{b} = \begin{cases} \frac{1}{\lambda_l}\left(1 - \frac{0.055(3 + \psi)}{\lambda_l}\right) & \text{for internal compression element} \\ \frac{1}{\lambda_l}\left(1 - \frac{0.188}{\lambda_l}\right) & \text{for outstanding compression element} \end{cases}$$

(1)

with $\quad \lambda_l = \sqrt{f_y / \sigma_{cr}}$

(2)

In Eq. (1) ρ is the reduction factor on the plate width and b and b_e are the total and the effective width of the plate, respectively. The slenderness ratio λ_l relates the material yield stress f_y to the elastic local buckling stress of the plate σ_{cr} and ψ is the ratio of the end stresses in the plate. Eurocode 3 calculates the effective cross-section A_{eff} using the yield stress f_y in Eq. (2). The calculation of the effective cross-section in bending is an iterative process, since the neutral axis of the effective cross-section shifts by an amount dependent on the reduction of the effective section (in the flange and upper portion of the web), which in turn affects the stress distribution. Although not required by EC3 guidelines, full iterations to convergence were carried out in this study.

2.2. Distortional buckling

Distortional buckling of CFS members is defined by the distortion of

the shape of the cross-section excluding the deformations related to local buckling (Fig. 2(b)). The EC3, Part 1.3 [23] design method for distortional buckling is based on the assumption that the effective parts of the edge stiffener behave as a strut element continuously supported by elastic springs of stiffness K along its centroid axis, as shown in Fig. 4(b). The buckling behaviour of the section can then be studied by considering an equivalent strut on an elastic foundation with the critical buckling stress calculated as:

$$\sigma_{cr,s} = \frac{2\sqrt{KEI_S}}{A_S}$$

(3)

where K is the spring stiffness per unit length; and A_S and I_S are the area and effective second moment of area of the stiffener, respectively. The flexural buckling resistance of a stiffener is then obtained by multiplying $A_S \cdot \sigma_{cr,s}$ by a reduction factor χ_d, which is defined in Fig. 4(c).

It is worth noting that EC3, Part 1.3 [23] considers the interaction of local/distortional buckling by reducing the thickness of the effective parts of the stiffener to t_{red}. Also, the local buckling plate slenderness λ_p for flange and lip is updated by considering the distortional buckling slenderness by:

$$\lambda_{p,red} = \lambda_p \sqrt{\chi_d}$$

(4)

For each step, the plate effective width is refined until $\chi_{d,n-1} \approx \chi_{d,n}$ but $\chi_{d,n} \leq \chi_{d,n-1}$. The iteration is optional in EC3.

3. Direct Strength Method (DSM)

The Direct Strength Method (DSM) is a finite strip-based method that integrates stability analysis into the design process. First the elastic local (M_{crl}), distortional (M_{crd}) and global (M_{cre}) critical buckling moments of CFS members are calculated using software such as CUFSM [9]. The equations for calculating the nominal flexural strength for global buckling (M_{ne}) are a function of the flexural yield moment $M_y = W_y \cdot f_y$ and the critical elastic lateral-torsional buckling M_{cre}:

$$\begin{aligned} M_{ne} &= M_{cre} & \text{for} \quad M_{cre} < 0.56 M_y \\ M_{ne} &= \frac{10}{9} M_y \left(1 - \frac{10 M_y}{36 M_{cre}}\right) & \text{for} \quad 2.78 M_y \geq M_{cre} \geq 0.56 M_y \\ M_{ne} &= M_y & \text{for} \quad M_{cre} \geq 2.78 M_y \end{aligned}$$

(5)

The nominal flexural strength of a CFS beam designed for local buckling (M_{nl}) and considering local–global interaction is related to the local–global slenderness $\lambda_l = \sqrt{M_{ne}/M_{crl}}$:
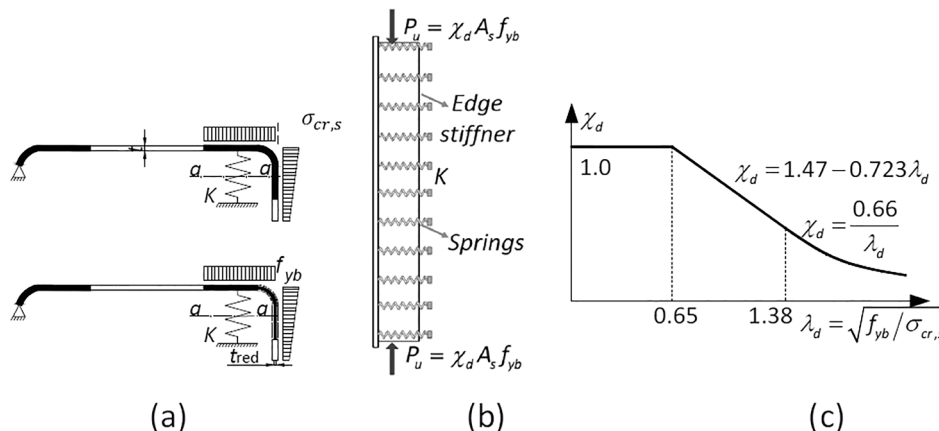

Fig. 4. Distortional buckling model (a) flange with edge stiffener; (b) flexural buckling of edge stiffener as a strut on elastic foundation; and (c) flexural buckling curve for edge stiffener.
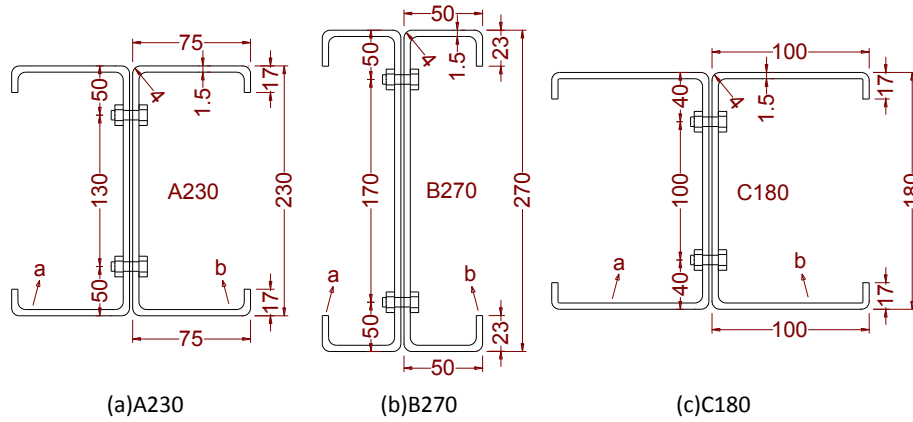
Fig. 5. Symbol definitions and nominal cross-sectional dimensions for the specimens (a) A230, (b) B270, and (c) C180.

$$\begin{cases} M_{nl} = M_{ne} & for \ \lambda_l \leq 0.776 \\ M_{nl} = \left[1-0.15\left(\frac{M_{crl}}{M_{ne}}\right)^{0.4}\right]\left(\frac{M_{crl}}{M_{ne}}\right)^{0.4}\cdot M_{ne} & for \ \lambda_l > 0.776 \end{cases}$$

(6)

The nominal flexural strength for distortional buckling (M_{nd}) is then calculated as a function of slenderness :

$$\begin{cases} M_{nd} = M_y & for \ \lambda_d \leq 0.673 \\ M_{nd} = \left[1-0.25\left(\frac{M_{crd}}{M_y}\right)^{0.6}\right]\left(\frac{M_{crd}}{M_y}\right)^{0.6}\cdot M_y & for \ \lambda_d > 0.673 \end{cases}$$

(7)

Finally the flexural strength of the CFS beam is determined based on the minimum value calculated from Eqs.(6)–(8):

$$M_n = \min\{M_{ne}, M_{nl}, M_{nd}\} \tag{8}$$

4. Selection of specimens

An optimisation framework proposed by the authors [24,25] is adopted for the selection of CFS back-to-back channel section for test and numerical study. The objective function is to obtain a design solution with maximum bending capacity but within the deflection criteria:

$$\max \ M_{c,Rd} = \chi_{LT}\cdot W_{eff}\cdot f_y \tag{9}$$

subject to EC3 width-to-thickness ratio limits [23], manufacturing constraints and deflection criteria:

$$b/t \leq 60, \quad c/t \leq 50, \quad h/t \leq 50 \tag{10}$$

$$0.2 \leq c/b \leq 0.6 \tag{11}$$

$$b \geq 50, \quad c \leq 25 \tag{12}$$

$$\Delta < \Delta_{lim} \tag{13}$$

where h is the cross-sectional height, and b and c are the flange and lip width, respectively. W_{eff} is the effective modulus of the cross-section considering the local/distortional buckling. χ_{LT} is the reduction factor taken into account the lateral-torsional buckling. f_y is the yield stress of the material used.

Eq.(13) imposes a constraint on the upper limit of deflection $\Delta_{lim} = L/200$ (L = 1200 mm is the beam span) of the CFS beams [26]. A load factor of $1/1.35 = 0.74$ is used when calculating the deflections using effective cross-section according to EC3, Part 1.5 and Part 1.3 [22,23], which means the deflection is obtained by using a moment ratio of $M_s = 0.74M_{c,Rd}$. This is due to the fact that in the ultimate limit state design of CFS beams, the partial factor of 1.35 is used for the dead load while 1.5 is used for the live load. However, these partial factors are 1.0 for serviceability limit state design. A load factor of 1/1.35 = 0.74 means a slightly larger deflection will be calculated which

can be in the safe side. When calculating the deflection, a uniform bending moment is applied at both ends of a simply-supported beam.

Fig. 5 shows the nominal dimensions of the three different cross-sections used in this study. All the dimensions in this figure are in *mm* and are defined between the outer to outer surfaces. The cross-section A230 is a standard commercially available cross-section, while section B270 is the optimum solution with the highest flexural strength subject to the constraints in Eqs.(10)–(13). Cross-section C180 (with a flange width larger than the flange widths of sections A230 and B270) is used for comparison purposes. All cross-sections have the same nominal thickness $t = 1.5$ mm and coil width of steel sheet $l = 415$ mm to use the same amount of material. The values for the radius of the round corner, the elastic modulus and the Poisson's ratio used were taken as 3 mm, 210 GPa and 0.3, respectively. The yield stress of the CFS material was considered to be $f_y = 450$ MPa in the optimisation process.

5. Numerical modelling

The above three sections were manufactured using the press breaking process and were tested about their major axis using a four-point bending set-up as shown in Fig. 6 to obtain their flexural strength. For each cross-section, two similar specimens with the same cross-section were tested to ensure the consistency of the results. The non-linear stress-strain behaviour and enhanced corner properties of the material were obtained based on the results of six tensile coupons. Tensile coupons were extracted from both the flat and the corner regions of the cross-sections to determine the material properties. The geometric imperfections of the back-to-back specimens were recorded using a specially designed measurement rig. More information about the conducted experimental tests can be found in [27].

5.1. Material model

The inelastic properties of CFS material were found to have significant effects on the ultimate capacity and post-buckling behaviour of CFS beams [28]. In this study, the results of the six tensile coupon tests from the flat plates and round corner regions of the cross-sections were used to investigate the effects of the forming process on the material properties. For example, a comparison between the engineering and true stress-strain curves of a flat and a corner coupon is given in Fig. 7 for the standard A230 section. The results indicate that the 0.2% proof stress of the corner coupon is around 24% higher than that of the flat coupon in the same section. Moreover, a comparison between the dynamic and static stress–strain curves of the coupon specimens shows that the stress reduced by around 5–8% at both yield and ultimate strengths during the static drop in the curves, which is also called "stress relaxation" [29]. The static stress–strain curves are calculated from the dynamic stress–strain curves by removing the dynamic effects
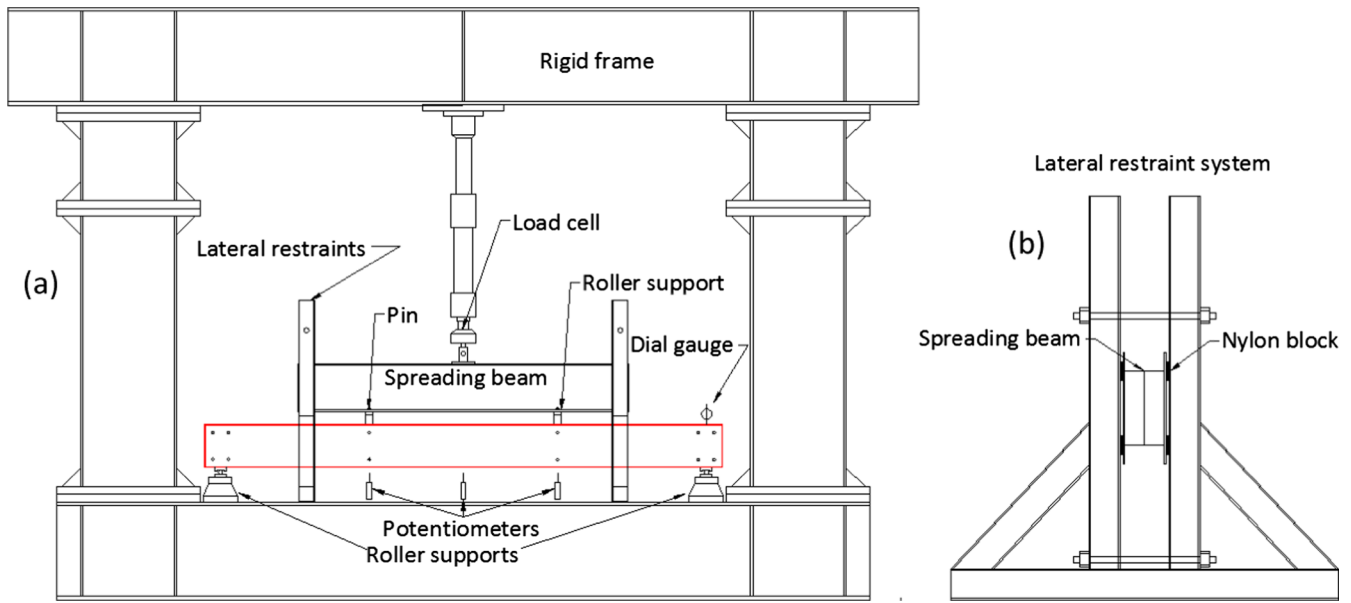
Fig. 6. Typical experimental set-up of four-point bending tests of back-to-back beam sections.
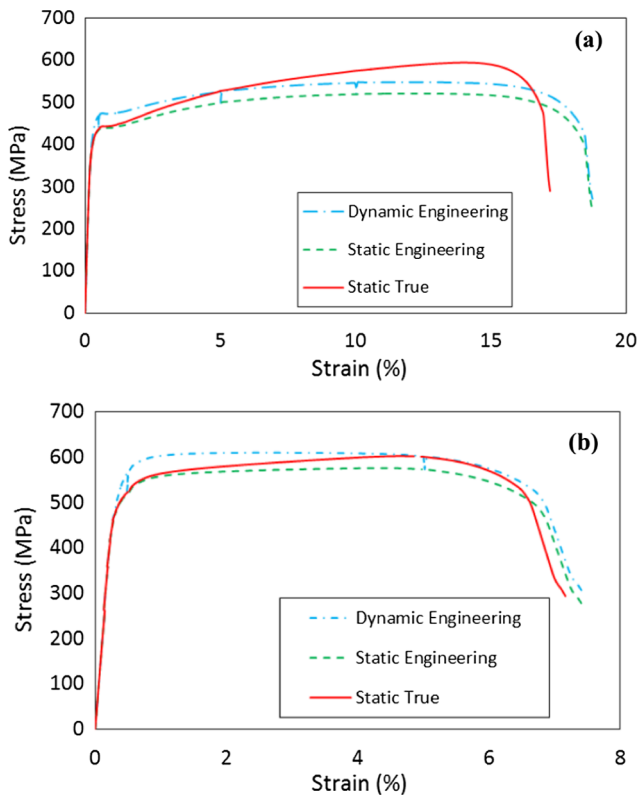

Fig. 7. Stress–strain curves resulted from (a) flat and (b) corner coupon tests.

of the tensile test. The material model was then included in the FEM by using the true stress vs true strain curve, which was calculated from the following equations:

$$\sigma_{true} = \sigma(1 + \varepsilon) \quad (14)$$

$$\varepsilon_{true} = \ln(1 + \varepsilon) \quad (15)$$

where σ and ε are the measured engineering stress and strain, respectively, based on the original cross-section area of the coupon specimens.

The resulting stress-strain curves for both the flat plates and round corner areas were also incorporated into ABAQUS [12].

Residual stresses were not included in the numerical model. It has previously been demonstrated that the effects of membrane residual stresses can safely be neglected in open sections [10,28], while the (longitudinal) bending residual stresses have been implicitly considered in the coupon test results, provided that the coupons are cut from the fabricated cross-section rather than from the virgin plate. Indeed, cutting a coupon releases the bending residual stresses, causing the coupon to curl [30]. However, these stresses are re-introduced when the coupon is straightened under tensile loading in the initial stages of the coupon test.

Previous studies also proposed that the effect of residential stress is relatively minor on the ultimate capacity [10,28]. The residual stress in the numerical modelling is therefore ignored in this paper. However, considering the strain hardening without introducing the residual stress may lead to slightly unconservative results.

5.2. Boundary conditions

The CFS back-to-back beams were tested in a four-point bending configuration, as illustrated in Fig. 6(a). The specimens were supported on rollers located 3100 mm apart. All specimens were bent about their major axis. The load was applied through a spreader beam onto the test specimens at two discrete locations 1200 mm apart. The spreader beam was restrained against any out-of-plane movement by a specially designed guidance system, as shown in Fig. 6(b). Nylon blocks were used as bearing pads between the spreader beam and the uprights in order to reduce vertical friction. A pin and a roller support were used to transfer the load from the spreader beam to the specimen. These supports were also designed to restrain the longitudinal displacement of the top flange of the test specimen and the spreading beam. To simulate the boundary conditions of the experimental program, a simply supported condition was used at both ends of the FE models as shown in Fig. 8. Two reference points were established at the positions of the roller and pin supports at the middle of the gap between the top two flanges of the CFS back-to-back beams to apply the external loads. The nodes under the region of the supports were coupled to the related reference point corresponding to the pin and roller supports as indicated in Fig. 8.

In order to avoid the localised bearing failure of the CFS sections during the experimental tests, wooden blocks were packed into the
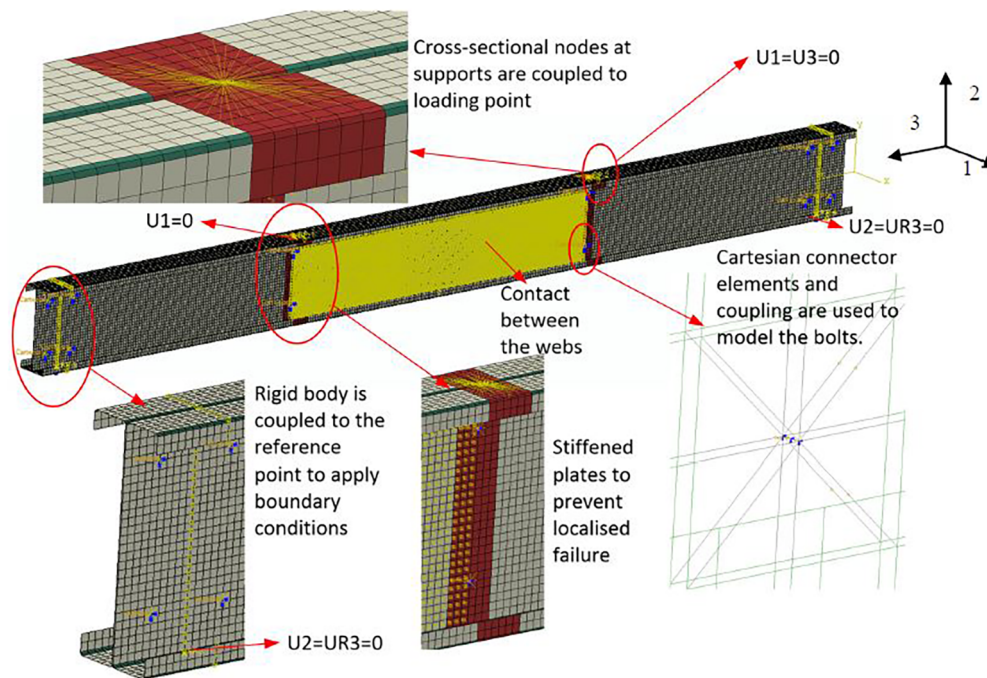
Fig. 8. Boundary conditions of FE model against test.

cross-section at the loading points and the end supports (see Fig. 6). Therefore, in the FE models, the elastic modulus of 10*E* was used for the steel plates in the areas with the wood blocks to simulate the rigid behaviour. A rigid body constraint, with a reference point at the middle of the gap between the two bottom flanges of the CFS back-to-back beams, was used at both ends of the CFS beam to prevent localised failure at the supports. To simulate the roller supports at the two ends of the CFS beams, the translational and rotational degrees of freedoms at the reference points were set to be U2 = UR3 = 0 (see Figs. 6 and 8). Regarding the reference points at the loading positions, the translations of U1 and U3 were fixed at the pin support while U1 = 0 was used at the roller support. This was to prevent the lateral deformation and longitudinal displacement of the CFS beams at these locations.

The CFS back-to-back beams were assembled by using two single channels with bolts as shown in Fig. 5. A connector element was used to model the bolt behaviour as will be explained in Section 5.4. Contact pairs were also defined between the two webs of each CFS single channel section using a surface-to-surface contact property. In the normal direction of the contact pairs, a "hard" surface was used while in the tangent direction between the two profiles a "frictionless" property was defined.

5.3. Element type and mesh size

A four-node, quadrilateral shell element (S4R) with reduced integration and hourglass control was used for the modelling of the CFS beams. This shell element can take into account transverse shear deformations and has been successfully used in the modelling of CFS beam sections by other researchers [7,8,20].

The effects of mesh size in the FE model on the behaviour of the CFS beams were firstly investigated. It was found that using a 10×10 mm element dimension for the CFS channels provides a balance between computational time and accuracy. Therefore, 10×10 mm elements were used for all FE simulations in this study. However, for the modelling of the corners of the CFS sections, it was found that two elements were suitable for the modelling of each round corner.

5.4. Modelling of bolts

It was found from reference experimental tests [31–33] that the position and behaviour of bolts can considerably influence the moment-rotation behaviour of the back-to-back CFS beams. The failure mode of the tested beams was also demonstrated to be significantly affected by the bolt slippage and bearing deformation. Therefore, it is important to develop an appropriate model in ABAQUS to simulate the local load-deformation behaviour of a single bolt bearing against a single steel sheet. Lim and Nethercot [2,3] used a simplified bolt model which consisted of two perpendicular nonlinear springs to model the bearing behaviour of a single bolt. In their study, good agreement was achieved between experimental test results and the modelled behaviour of CFS full-scale joints subjected to monotonic load. A more direct method to model bolt behaviour using FE analysis is to use solid brick element and surface-to-surface contact interactions in ABAQUS [34–36]. The disadvantage of this model is that using solid elements makes the model more complex and, therefore, reduces the computational efficiency, especially in models with a large number of bolts. In addition, due to the presence of bolt rigid body movement and slippage, convergence could also be an issue [36]. A practical technique is therefore presented here to simulate the slippage and bearing behaviour of the bolts in CFS back-to-back sections.

For CFS back-to-back channels assembling, a fastener tension (pre-loading force) is applied to the head of the bolt by using a torque wrench. The torque–preloading relationship is often simplified by using a constant K, known as the torque coefficient, as shown in the following equation [37,38]:

$$T = K \cdot P_b \cdot d \tag{16}$$

where T (N·mm) is the input tightening torque applied to the fastener head or nut, P_b (N) is the preloading force and d (mm) is the nominal bolt diameter. An approximate value of 0.2 has been used for the torque coefficient [37,38]. This results in an equivalent preloading force of $P_b = 6.25$ kN, which is close to the results presented by Croccolo et al. [39]. The slippage behaviour of the bolts depends mainly on the distribution of initial friction forces, which in return relies on the bolt pretension force P_b for a given applied torque and friction coefficient μ
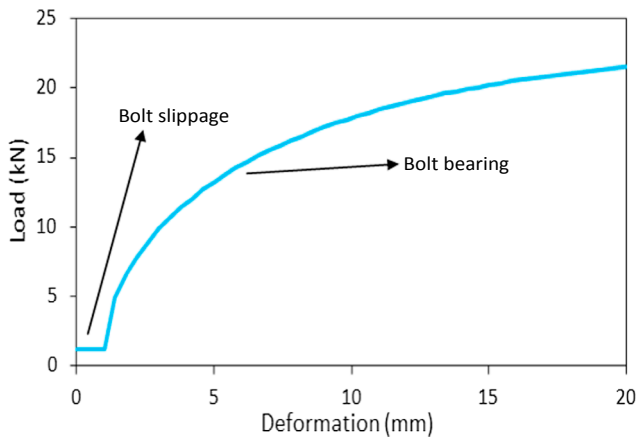
Fig. 9. Load-deformation relationship of a bolt slipping and bearing against a steel plate.

of the contact surfaces. The following formula is used to calculate the bolt slip resistance F_{slip} [40]:

$$F_{slip} = \mu \cdot P_b \cdot n_b \tag{17}$$

where μ is the mean frictional coefficient taken as 0.19 for galvanised steel surfaces [40], and n_b is the number of slip planes.

A single bolt can transfer shear forces to a CFS member through the bearing behaviour in addition to slippage described above. Once the slippage deformation overcomes the gap between the bolt shank and the steel sheet, the bearing behaviour of the bolt against steel sheet will be activated. Fisher [41] proposed the following equation to take into account the bolt bearing force and the bearing deformation relationship:

$$R_B = R_{ult} [1 - e^{-\mu(\delta_{br}/25.4)}]^\lambda \tag{18}$$

$$R_{ult} = 2.1 \cdot d \cdot t \cdot F_u \tag{19}$$

where δ_{br} is the bearing deformation (mm), R_{ult} is the ultimate bearing strength, t is the web thickness, d is the bolt diameter and R_B is the bearing force against the bearing deformation. F_u is the tensile strength of the web plate material, which can be obtained from coupon tests. $e = 2.178$ is the nature exponential, while $\mu = 5$ and $\lambda = 0.55$ are the regression coefficients presented by Uang et al. [42].

In the reference experimental tests [27], the bolt shank diameter

was 12 mm. The bolt slippage behaviour is generally defined for a limited range of slip movement within the bolt hole clearance (typically ± 1 mm for standard bolts by assuming that the bolt shanks are centrally positioned). According to Eqs. (16)–(19), a slip-bearing relationship can be defined as shown in Fig. 9. The slip-bearing relationship has been successfully used to model the cyclic behaviour of bolted moment connections by Ye [27].

In order to model a group of bolts, the connector element in ABAQUS [12] was used, as shown in Fig. 10(a). For each single bolt in Fig. 10(a), a two-layer fastener configuration was used at the position of each individual bolt in the full-scale connection (see Fig. 10(b)). The layer was connected by a node in one channel section and a point in its counterpart section using a connector element to define the bolt property. The connector type of "Cartesian" with 3 translational degrees of freedom at each node was employed. This connector was characterised by a parallel combination of "Elasticity" and "Plasticity" behaviours, as defined in ABAQUS [12]. In the "Elasticity" behaviour, the rigid definition was used in the corresponding shear direction. For the definition of "Plasticity" behaviour, the load-deformation relationship shown in Fig. 9 was employed to represent the behaviour of a bolt which is slipping and bearing against a steel plate. It should be noted that the "Elasticity" and "Plasticity" behaviours are defined in local coordinate systems corresponding to the shear deformation of the bolts.

The bolt slippage and bearing behaviour, which are defined in Eqs. (16)–(19), are included in the connector element shown in Fig. 10(a). Therefore, it is important to exclude the bearing deformation stemmed from the bearing of each node at the bolt position. To achieve this, constraints "Coupling" in ABAQUS [12] was employed, and its definition is shown in Fig. 10(b). Each node at the position of the bolts was thereby connected to the nearby nodes in the CFS steel plates using the constraint that couples the displacement and rotation. These nodes should lie in a reasonably large region in the plates to reduce the bearing deformation.

5.5. Imperfections

The stability of thin-walled CFS members may in some cases be significantly affected by the presence of imperfections, especially when interactive buckling of different modes is involved. In the reference experimental programme, the magnitude and the shape of the geometric imperfections of each specimen were therefore recorded before testing. The imperfections were measured along the five longitudinal lines indicated in Fig. 11(a), by means of reflected laser beams. As a first step, the raw data were decomposed into its respective Fourier
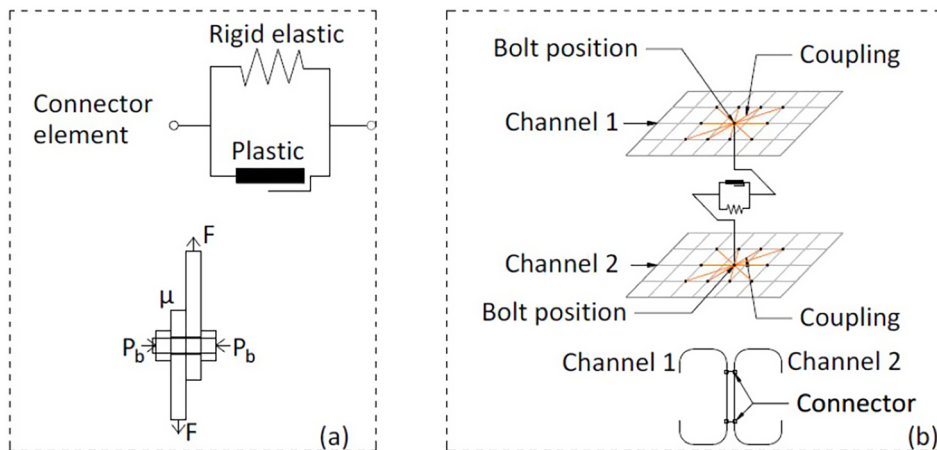

Fig. 10. Single bolt modelling in ABAQUS: (a) components defined in a connector; (b) reducing the bearing behaviour by coupling the node at the bolt position to a number of nodes close-by.
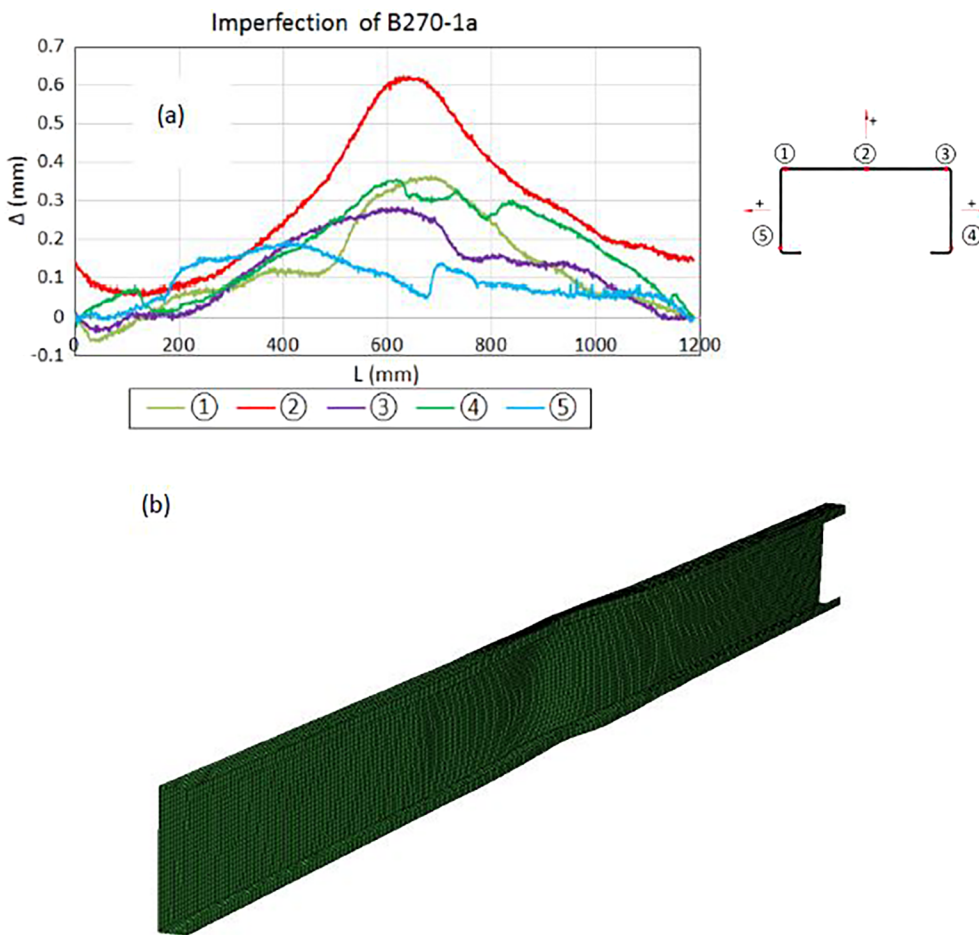
Fig. 11. Measured imperfection of B270-1a (a) profiles; (b) included in the FE model (magnified 50 times).
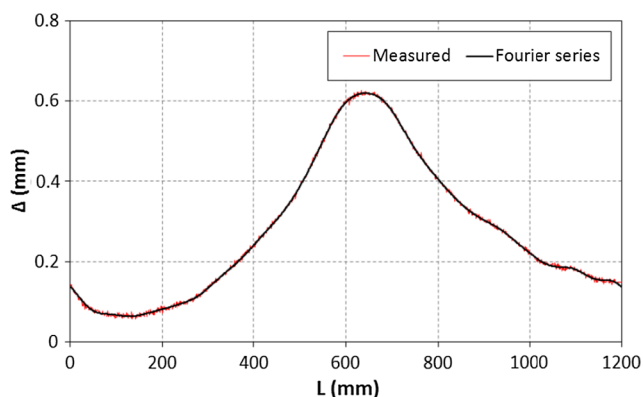

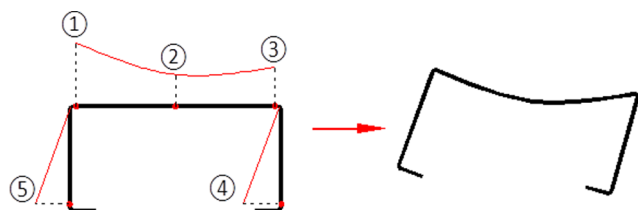Fig. 12. Measured imperfection profile and its Fourier representation.

Fig. 13. Imperfection inclusion.

series and a finite number of terms were removed to cut off the high frequency vibrations originating from the driving mechanisms of the moving motors. Using this reduced Fourier series resulted in a more continuum node coordinates adjustment when the measured imperfections were included.

It should be noted that in general, it is essential to use a sufficient number of Fourier terms to represent the shape of the measured imperfections. In this study, by inspection, it was found that using 20 Fourier terms typically leads to accurate results. As an example, Fig. 12 compares the measured imperfection profile along line 3 of specimen B270-1a, with the truncated Fourier representation shown as a solid black line. Within a given cross-section, the magnitude of the imperfection at each node of the FE mesh was determined by interpolation of the measurements. Quadratic interpolation was used for the web imperfections, while linear interpolation was used at the flanges, as show in Fig. 13. The coordinates of each node in the FE models were then adjusted to account for the imperfections.

5.6. Numerical results

Table 1 compares the ultimate load carrying capacities resulting from the FE models against those obtained from the reference experiments on the CFS lipped channel beams with different cross-sections. M_{u1} is the predicted flexural strength that takes into account the strain hardening effect of the material in the corner region but without incorporating the geometric imperfections. M_{u2} indicates the predicted moment capacity where only the effect of the measured initial geometric imperfections was taken into account. The predicted capacity M_{u3}, on the other hand, considers both the measured initial geometric

Table 1
Comparison of FE results with tested flexural strength.

Specimen	M_u (kN·m)	M_{u1} (kN·m)	M_{u2} (kN·m)	M_{u3} (kN·m)	M_{u1}/M_u	M_{u2}/M_u	M_{u3}/M_u
A230-1	23.72	25.31	23.12	23.94	1.067	0.975	1.009
A230-2	23.79	25.58	22.39	23.92	1.075	0.941	1.005
B270-1	(25.83)	28.87	25.95	26.11	–	–	
B270-2	28.34	28.25	27.82	28.47	0.997	0.982	1.005
C180-1	17.43	18.22	16.41	17.68	1.045	0.941	1.014
C180-2	17.24	17.89	16.53	17.55	1.038	0.959	1.018
Average					1.044	0.960	1.010
St. Dev.					0.031	0.019	0.006

Note: M_u is the tested flexural strength, M_{u1} is the predicted flexural strength considering the strain hardening effect of the material in the corner region, M_{u2} indicates the predicted moment capacity where only the effect of the measured initial geometric imperfections was considered, M_{u3} is the predicted capacity considering measured initial geometric imperfections and the strain hardening effect of the material in the corner regions.

imperfections and the strain hardening effect of the material in the corner regions.

As shown in Table 1, excellent agreement was obtained between experimental results and FE predictions. The average ratio of the FE predicted bending capacity M_{u2} to the experimentally measured flexural strength M_u was 0.960, with a standard deviation of 0.019. In comparison, the average ratio of the FE predicted bending capacity M_{u3} to the experimentally measured load carrying capacity M_u was 1.010, with a standard deviation of 0.006. This indicates that considering the strength variation caused by the strain hardening effect of the round corner material, this could change the accuracy of the bending capacity predictions by 5%. However, by comparing the predicted flexural strength M_{u1} with M_{u3}, it is shown that the initial geometric imperfections can have up to a 7% effect on the load carrying capacity. It should be noted that, on average, the variation of flexural strength is 3.1% and 0.6%, with and without taking into account the geometric imperfections, respectively.

Fig. 14 illustrates the tested moment versus mid-span deflection curves corresponding to the reference experimental tests and the predicted results from numerical study. It is shown that the proposed FE model was able to capture the peak load and stiffness of CFS beam sections with a very good accuracy.

Fig. 15 compares the failure shapes of the tested specimens with the predicted deformation of the corresponding FE models. It is shown that the proposed FE model could also predict well the failure modes of the CFS beams. As presented in Fig. 15(a)–(c), in the numerical models, all specimens failed within the constant moment span by interaction of local and distortional buckling. In specimens C180-1 and C180-2, pure local bucking firstly happened in the top flanges. This was due to the high slenderness of the flanges, which had a width-to-thickness ratio of 67, and the fact that they were subjected to the highest compressive stress in the cross-section. As the bending moment increased, superimposed distortional buckling was observed in the numerical models, as shown in Fig. 15(a). Participation of the webs was also captured before the ultimate capacity of the specimens was reached.

It is shown in the numerical models that beams A230-1 and A230-2 failed due to interaction between local and distortional buckling, as shown in Fig. 15(b). However, due to the higher slenderness of the web, the local buckling was first triggered in the web rather than the flange. As the load increased, distortional buckling mode was observed as well.

The beams B270-1 and B270-2 had the maximum web height, combined with relatively narrow flanges. Local buckling was again first detected in the webs of the channels in the numerical models, with distortional buckling participated at a higher load level (see Fig. 15(c)).
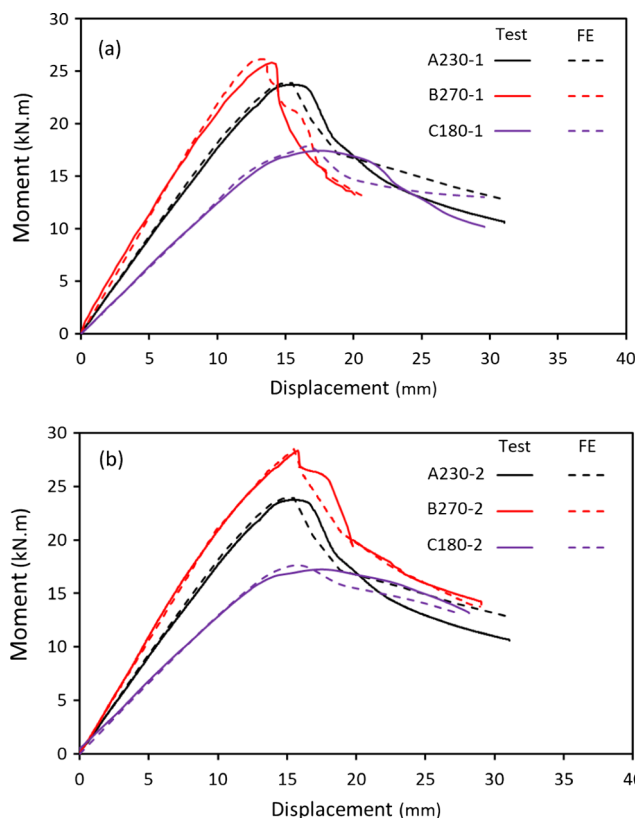

Fig. 14. Moment versus mid-span deflection relationship resulting from FE against Test.

These results discussed above in general confirm the adequacy of the developed FE models in simulating the actual behaviour of CFS back-to-back beam channels up to their failure points.

6. Evaluation of current design methods

In this section, the experimental results are compared to the predictions of the DSM and EC3 design equations presented in Section 2 and 3. The specimen B270-1 was tested without the wood blocks and was failed by a localised failure at the top flange rather than the expected bending failure. Therefore, the result of specimen B270-1 was not considered here. As shown in Table 2, both DSM and EC3 predictions on the bending capacity of CFS back-to-back beams were accurate enough for practical design considerations. The ratio of the DSM predicted load capacity to the experimentally measured load carrying capacity was 0.96, with a standard deviation of 0.05. It is evident from Table 2 that the "effective width" based method comprised in EC3 generally leads to accurate predictions (on average 99% with a standard deviation of 9%) of the beam strengths. However, the EC3 results in some cases can be up to 10% overestimated.

By comparing the ultimate bending capacity of the standard and optimised sections for the CFS beams obtained from the experimental results (shown in Table 2), detailed FE models and EC3 design method. Based on the experimental results, it can be seen that the optimised shapes (B270) offer a much higher flexural strength (up to 19% higher) compared to the standard lipped channel section with the same amount of material. Similar results were obtained from FE models and EC3 design method, where the optimum design solutions showed around 20% higher flexural strength compared to the standard sections.
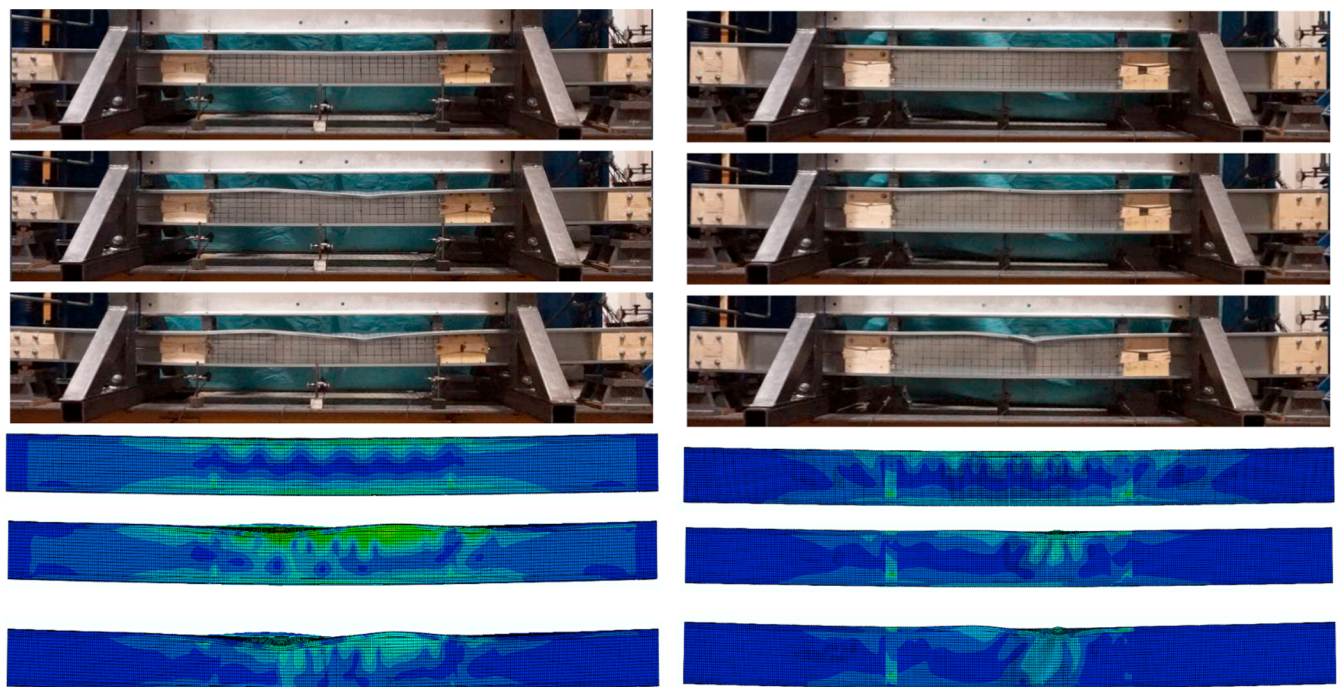
(a) Failure progression in beam C180-2

(b) Failure progression in beam A230-2
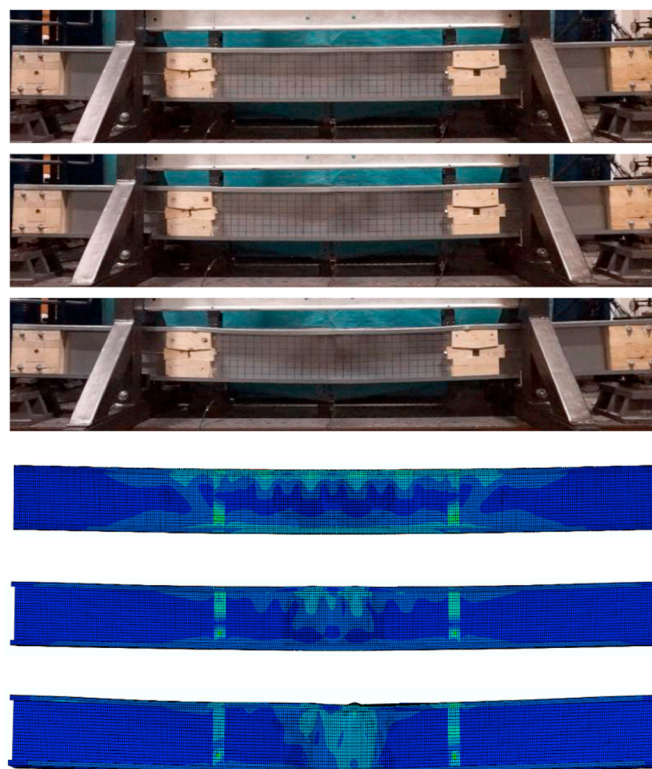
(c) Failure progression in beam B270-2

Fig. 15. Failure progression and deformation of FE model vs actual specimen and for the tested beams (a) C180-2, (b) A230-2, (c) B270-2.

7. Determine deflections of CFS back-to-back beams

Serviceability criteria should be also taken into account in CFS beam design, especially for supporting beams in long span roof or floor systems. Eurocode 3 Part 1-3 stipulates that the effective cross-section for the serviceability limit state should be used in all serviceability limit state calculations for CFS members. In determination of the cross-sectional properties of CFS sections, the effective parts of individual plates in the cross-section will be different according to the stress levels obtained from the distribution of bending moments. Meanwhile, the deflections are generally estimated by using the secant modulus of elasticity, especially in alloys with pronounced strain hardening behaviour.

To predict the deflections of the tested beams, six different cases (including the method suggested by EC3) were considered by varying the material nonlinearity (using the secant modulus of elasticity, see Fig. 7) and moment gradient along the beam span. The results were then compared with those obtained from the reference experimental tests. This well help to assess the errors associated with any of these simplifying assumptions and identify the best practical method to calculate the deflection of CFS beams:

Method 1: Calculation of deflections using a constant modulus of elasticity (E_{s0}) at the initial stage of the nonlinear stress-strain curve, and gross cross-section properties (I) along the length of the beam.

$$d = \int_0^{L_1} \frac{M(x) \cdot x}{E_{s0} \cdot I} dx \tag{20}$$

where d is the calculated deflection, $M(x)$ is the bending moment at the position of x and L_1 is the beam span to be considered.

Method 2: Assuming constant modulus of elasticity (E_{s0}) at the initial stage of the nonlinear stress-strain curve to calculate the deflections, but with the effective cross-sectional property $I_{eff,max}$ determined at the maximum stress level along the beam span:

$$P \to M_{max} \to \sigma_{gr,max} \to b_{eff} \to I_{eff,max} \to d = \int_0^{L_1} \frac{M(x) \cdot x}{E_{s0} \cdot I_{eff,max}} dx \tag{21}$$

Method 3: Calculation of deflections using the constant modulus of elasticity (E_{s0}) at the initial stage of the nonlinear stress-strain curve but considering the variation of the effective cross-sectional properties $I_{eff}(x)$ at various stress levels along the length of the beams.

$$P \to M = M(x) \to \sigma(x) \to b_{eff}(x) \to I_{eff}(x) \to d = \int_0^{L_1} \frac{M(x) \cdot x}{E_{s0} \cdot I_{eff}(x)} dx \tag{22}$$

Method 4: Calculation of deflections considering variation of modulus of elasticity ($E_s(x)$) along the length of the beam, but using the constant gross cross-sectional property (I) of the beams.

$$P \to M = M(x) \to \sigma(x) = \frac{M(x)}{W} \to \varepsilon(x) \to E_s(x) \to d = \int_0^{L_1} \frac{M(x) \cdot x}{E_s(x) \cdot I} dx \tag{23}$$

Method 5: Calculation of the deflections considering the variation of modulus of elasticity ($E_s(x)$) along the length of the beam, and a change of effective cross-sectional property $I_{eff}(x)$ at various stress levels along the length of the beam:

$$P \to M = M(x) \to \sigma(x) = \frac{M(x)}{W} \to b_{eff}(x) \to \varepsilon(x) \to E_s(x) = \frac{\sigma(x)}{\varepsilon(x)} \to d = \int_0^{L_1} \frac{M(x) \cdot x}{E_s(x) \cdot I_{eff}(x)} dx \tag{24}$$

Method 6: Calculation of the deflections using the Eurocode suggested methodology. The variation of the effective second moment of area I_{fic} is taken into account by using an interpolation between gross cross-sectional property I_{gr} and effective cross-section property $I(\sigma_{eff,max})_{eff}$ determined at the maximum stress level $\sigma_{eff,max}$ using the effective cross-section along the beam:

$$I_{fic} = I_{gr} - \frac{\sigma_{gr}}{\sigma_{eff,max}} (I_{gr} - I(\sigma_{eff,max})_{eff}) \tag{25}$$

Table 2
Evaluation of the DSM and EC3 design methods to predict the bending capacity.

Specimen	Test (kN·m)	EC 3 (kN·m)	DSM (kN·m)	EC3/Test	DSM/Test
A230-1	23.72	22.38	22.42	0.94	0.95
A230-2	23.79	22.59	22.61	0.95	0.95
B270-1	(25.83)	25.26	25.76	–	–
B270-2	28.34	25.09	25.38	0.89	0.90
C180-1	17.43	18.77	17.42	1.08	0.99
C180-2	17.24	18.91	17.40	1.10	1.01
Average				0.99	0.96
St. Dev.				0.09	0.05

The calculation process is shown below using the constant modulus of elasticity (E_{s0}) at the initial stage of the nonlinear stress-strain curve:

$$P \to M \to \sigma_{gr} \to I_{gr} \to b_{eff} \to I_{eff} \to \sigma_{eff,max}$$
$$\to b_{eff}(\sigma_{eff,max}) \to I(\sigma_{eff,max})_{eff} \to I_{fic} \to d = \int_0^{L_1} \frac{M(x) \cdot x}{E_{s0} \cdot I_{fic}} dx \tag{26}$$

The resulting deflections obtained for the tested beams, according to the methods presented in Eqs. (20)–(26) are analyzed. Fig. 16 presents the resulting load-deflection curves at mid span compared to the load-deflection relationships recorded in the experiments. The horizontal line is the load level used for the design of the CFS beams at serviceability limit state, as presented in Section 4.

A comparison between the calculated deflections using Methods 1 and 4, and similarly comparing Methods 3 and 5, shows that there is no significant difference between the results when the variation of secant modulus along the length of the beams is taken into account. This means that for the tested CFS beams, using the secant elastic modulus along the stress-strain curve have little effect on the determination of deflections, which agrees well with the EC3, Part 1-3, where no requirement is imposed on the secant modulus. The modulus of elasticity would be used for the design of the beams to serviceability limit state.

A comparison between the curves obtained from Methods 1 and 2 shows that the use of linear elastic properties for the cross-sections (i.e. full section properties) leads to underestimated deflections compared to the experimental results. The level of underestimation of deflection is 8% on average with a standard deviation of 2%, as shown in Table 3. When using reduced cross-sectional properties (I_{eff}) to calculate the deflections, Method 2 overestimates the deflections at the serviceability load. This is in line with the requirement of EC3, Part 1.3, where the effective cross-sections should be used in determination of the deflections.

A comparison between the results of Method 6 and the experimental measurements at the serviceability load level shows that, in general, the EC3, Part 1-3 overestimates the deflections to a reasonable level, which can be acceptable in the practical design of CFS beams. It is also shown in Table 3 that the deflections of both standard and optimised beams were within the limit of $L/200 = 15.5$ mm, as recommended in [26]. Based on the average and also standard deviation of the errors, Method 6 (EC3 suggested method) provides the most accurate estimations of the beam deflections under serviceability loads.

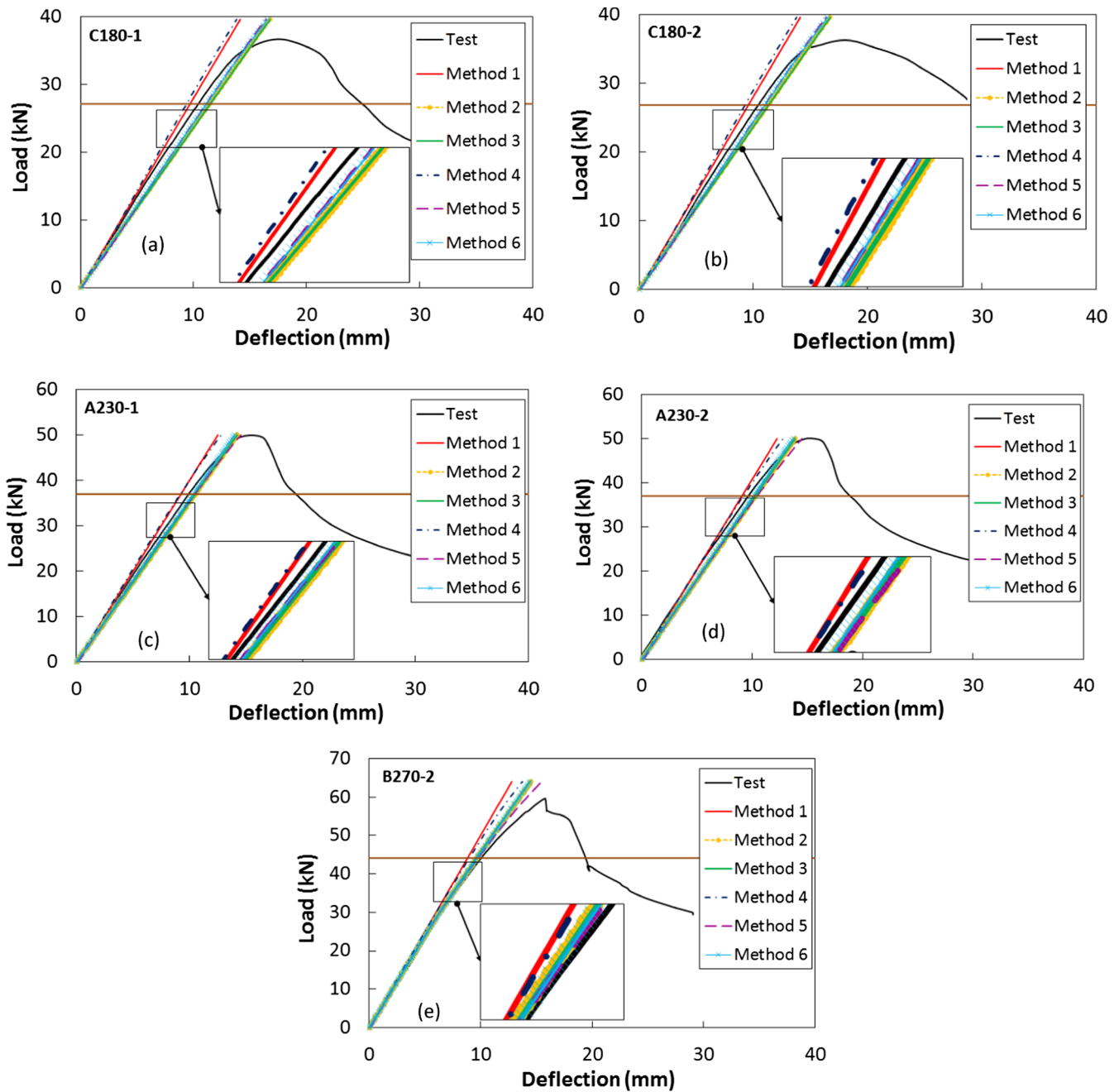It should be mentioned that for the CFS beams (3100 mm span) used

Fig. 16. Load-deflection curves at mid span calculated using various methods and the physical test for the tested beams (a) C180-1, (b) C180-2, (c) A230-1, (d) A230-2, (e) B270-2.

Table 3
Comparison of the experimental and calculated deflections using various methods at serviceability load.

Specimens	Test Δ_{test} (mm)	Method 1 Δ_1 (mm)	Method 2 Δ_2 (mm)	Method 3 Δ_3 (mm)	Method 4 Δ_4 (mm)	Method 5 Δ_5 (mm)	Method 6 Δ_6 (mm)	$\frac{\Delta_1}{\Delta_{test}}$	$\frac{\Delta_2}{\Delta_{test}}$	$\frac{\Delta_3}{\Delta_{test}}$	$\frac{\Delta_4}{\Delta_{test}}$	$\frac{\Delta_5}{\Delta_{test}}$	$\frac{\Delta_6}{\Delta_{test}}$
C180-1	10.4	9.7	11.5	11.5	9.4	11.1	11.2	0.93	1.11	1.11	0.90	1.07	1.08
C180-2	10.4	9.5	11.3	11.3	9.2	11.0	11.0	0.91	1.09	1.09	0.88	1.06	1.06
A230-1	9.9	9.2	10.5	10.5	9.1	10.4	10.3	0.93	1.06	1.06	0.92	1.05	1.04
A230-2	9.7	9.1	10.3	10.3	9.3	10.5	10.2	0.94	1.06	1.06	0.96	1.08	1.05
B270-2	9.9	8.9	9.7	9.7	9.0	9.9	9.7	0.90	0.98	0.98	0.91	1.00	0.98
Average								0.92	1.06	1.06	0.92	1.05	1.04
St. Dev.								0.02	0.05	0.05	0.03	0.03	0.04

in this study, it was found that the serviceability constraints have been automatically satisfied within the optimisation process, as shown in Table 3. This has been confirmed by both the experimental and numerical results. The deflection of the optimised cross-section (Cross-section B) at the serviceability load level is around 5% less than that of the standard cross-section (Cross-section A), according to Eurocode. The reason is that the optimised beam cross-sections generally tend to be with a larger profile height, which leads to a larger stiffness with reduced deflections.

8. Conclusions

An advanced numerical model has been developed to study the local/distortional buckling behaviour and deflections of CFS lipped back-to-back channel beams and to verify the efficiency of a previously proposed optimisation framework. The model takes into account the non-linear stress–strain behaviour of CFS material, the strain hardening effects at the round corners due to the cold-working process, and the experimentally measured initial geometric imperfections. The numerical model was validated against an experimental program on a total of 6 lipped channel back-to-back beams. The validated models were then used to assess the accuracy of EC3 and DSM design methods for standard and optimum design solutions. Based on the results presented in this paper, the following conclusions can be drawn:

(1) The ultimate capacity of the sections predicted by the FE models was on average less than 2% in variation from the experimental results. The proposed FE model was also successful in capturing the failure shapes and predicting the bending strengths of CFS back-to-back beams subject to local and distortional buckling modes. The numerical results also showed that local and distortional buckling was observed in all specimens while no lateral-torsional buckling was observed which agrees well with tests.
(2) Both DSM and EC3 resulted in accurate predictions of the beam flexural strengths. While DSM usually led to underestimated results, EC3 predictions were up to 10% overestimated with a standard deviation of 5% and 9%, respectively. Using EC3 reduced cross-sectional property to calculate deflections slightly overestimates the deflections at serviceability load. However, using linear elastic full cross-sectional properties provides consistent underestimation of the deflections (8% on average).
(3) The bending capacity of the optimised CFS beams obtained from validated FE models and EC3 design methods were up to 20% higher than standard lipped channel sections with the same amount of material. The previously proposed optimisation framework leads to cross-sections with higher web height, thus increased stiffness. The results demonstrate the efficiency of the adopted optimisation method to improve the bending capacity and stiffness of CFS sections.
(4) It was shown that, in general, taking the geometric imperfections into account can change the FE predictions by 7%. The strain hardening effects at the round corners due to the cold-working process can be ignored when improving the capacity and stiffness of CFS beams is the main objective.

Acknowledgments

Appendix A. Supplementary material

Supplementary data to this article can be found online at https://doi.org/10.1016/j.engstruct.2018.09.064.

References

[1] Fiorino L, Iuorio O, Landolfo R. Designing CFS structures: the new school bfs in Naples. Thin Wall Struct 2014;78:37–47.
[2] Lim JBP, Nethercot DA. Ultimate strength of bolted moment-connections between cold-formed steel members. Thin Wall Struct 2003;41:1019–39.
[3] Lim JBP, Nethercot DA. Finite element idealization of a cold-formed steel portal frame. J Struct Eng-ASCE 2004;130:78–94.
[4] Young B, Yan JT. Finite element analysis and design of fixed-ended plain channel columns. Finite Elem Anal Des 2002;38:549–66.
[5] Peköz T, Winter G, Desmond T. Edge stiffeners for cold-formed steel members. In: 4th international specialty conference on cold-formed steel structures; 1978.
[6] Desmond TP, Winter G, Pekoz T. Edge stiffeners for thin-walled members. J Struct Div 1981;107:329–53.
[7] Yu C, Schafer BW. Simulation of cold-formed steel beams in local and distortional buckling with applications to the direct strength method. J Constr Steel Res. 2007;63:581–90.
[8] Haidarali MR, Nethercot DA. Finite element modelling of cold-formed steel beams under local buckling or combined local/distortional buckling. Thin Wall Struct 2011;49:1554–62.
[9] Schafer B. CUFSM version 3.12. Department of Civil Engineering, Johns Hopkins University; 2006.
[10] Schafer BW, Pekoz T. Computational modeling of cold-formed steel: characterizing geometric imperfections and residual stresses. J Constr Steel Res 1998;47:193–210.
[11] Kankanamge ND, Mahendran M. Behaviour and design of cold-formed steel beams subject to lateral-torsional buckling. Thin Wall Struct 2012;51:25–38.
[12] Karlsson Hibbitt, Inc Sorensen, ABAQUS. ABAQUS/Standard user's manual volumes I-III and ABAQUS CAE manual. Version 6.12. (Pawtucket, USA), 2010.
[13] AS/NZS. Cold-formed steel structures. Sydney: AS/NZS 4600, Joint Technical Committee BD-082; 1996.
[14] AISI. North American specification for the design of cold-formed steel structural members. AISI S100-07. Washington, DC; 2007.
[15] CEN. Eurocode 3: Design of steel structures. Part 1–1: General rules and rules for buildings. Brussels: European Committee for Standardization; 2005.
[16] Keerthan P, Mahendran M. Numerical modeling of litesteel beams subject to shear. J Struct Eng-ASCE 2011;137:1428–39.
[17] Ayhan D, Schafer BW. Cold-formed steel member bending stiffness prediction. J Constr Steel Res 2015;115:148–59.
[18] Dubina D, Ungureanu V, Gîlia L. Cold-formed steel beams with corrugated web and discrete web-to-flange fasteners. Steel Constr 2013;6:74–81.
[19] Dubina D, Ungureanu V, Gilia L. Experimental investigations of cold-formed steel beams of corrugated web and built-up section for flanges. Thin Wall Struct 2015;90:159–70.
[20] Wang LP, Young B. Behavior of cold-formed steel built-up sections with intermediate stiffeners under bending I: Tests and numerical validation. J Struct Eng-ASCE 2016:04015150–4040151.
[21] Wang LP, Young B. Behavior of cold-formed steel built-up sections with intermediate stiffeners under bending. II: Parametric study and design. J Struct Eng-ASCE 2016. 04015151-04011.
[22] CEN. Eurocode 3: design of steel structures, Part 1. 5: Plated structural elements. Brussels: European Committee for Standardization; 2005.
[23] CEN. Eurocode 3: design of steel structures, Part 1. 3: General rules—supplementary rules for cold formed members and sheeting. Brussels: European Committee for Standardization; 2005.
[24] Ma WX, Becque J, Hajirasouliha I, Ye J. Cross-sectional optimization of cold-formed steel channels to Eurocode 3. Eng Struct 2015;101:641–51.
[25] Ye J, Hajirasouliha I, Becque J, Eslami A. Optimum design of cold-formed steel beams using particle swarm optimisation method. J Constr Steel Res 2016;122:80–93.
[26] Rhodes J. Design of cold formed steel members. Elsevier Appl Sci 1991.
[27] More Ye J. efficient cold-formed steel elements and bolted connections PhD thesis The University of Sheffield; 2016
[28] Schafer BW, Li Z, Moen CD. Computational modeling of cold-formed steel. Thin Wall Struct 2010;48:752–62.
[29] Huang YN, Young B. The art of coupon tests. J Constr Steel Res 2014;96:159–75.
[30] Jandera M, Gardner L, Machacek J. Residual stresses in cold-rolled stainless steel hollow sections. J Constr Steel Res 2008;64:1255–63.
[31] Serror MH, Hassan EM, Mourad SA. Experimental study on the rotation capacity of cold-formed steel beams. J Constr Steel Res 2016;121:216–28.
[32] Sabbagh AB, Petkovski M, Pilakoutas K, Mirghaderi R. Experimental work on cold-formed steel elements for earthquake resilient moment frame buildings. Eng Struct 2012;42:371–86.
[33] Sabbagh AB, Petkovski M, Pilakoutas K, Mirghaderi R. Cyclic behaviour of bolted cold-formed steel moment connections: FE modelling including slip. J Constr Steel Res 2013;80:100–8.
[34] Öztürk F, Pul S. Experimental and numerical study on a full scale apex connection of cold-formed steel portal frames. Thin Wall Struct 2015;94:79–88.
[35] Gutierrez R, Loureiro A, Reinosa JM, Lopez M. Numerical study of purlin joints with sleeve connections. Thin Wall Struct 2015;94:214–24.
[36] Liu Q, Yang J, Wang FL. Numerical simulation of sleeve connections for cold formed steel sigma sections. Eng Struct 2015;100:686–95.
[37] Juvinall RC, Marshek KM. Fundamentals of machine component design. New York: John Wiley & Sons; 2006.
[38] Bickford JH. An introduction to the design and analysis of bolted joints. New York: Marcel Dekker; 1997.

[39] Croccolo D, De Agostinis M, Vincenzi N. Failure analysis of bolted joints: effect of friction coefficients in torque–preloading relationship. Eng Fail Anal 2011;18:364–73.

[40] Wong MF, Chung KF. Structural behaviour of bolted moment connections in cold-formed steel beam-column sub-frames. J Constr Steel Res 2002;58:253–74.

[41] Fisher JW. On the Behavior of Fasteners and Plates with Holes. Fritz Engineering Laboratory, Department of Civil Engineering, Lehigh University; 1964.

[42] Uang CM, Sato A, Hong JK, Wood K. Cyclic testing and modeling of cold-formed steel special bolted moment frame connections. J Struct Eng-ASCE 2010;136:953–60.